Thermal excitation-energy deposition in 5–15 GeV/c hadron-induced reactions with ^{197}Au. II. Relation between excitation energy and reaction variables

L. Beaulieu,* T. Lefort,[†] K. Kwiatkowski,[‡] W.-c. Hsi,[§] G. Wang,[‖] D. S. Bracken,[‡] E. Cornell,[¶] D. S. Ginger,** K. B. Morley,[‡] and V. E. Viola
Department of Chemistry and IUCF, Indiana University, Bloomington, Indiana 47405

F. Gimeno-Nogues, R. Laforest,[††] E. Martin, E. Ramakrishnan,[‡‡] D. Rowland,[§§] A. Ruangma, E. Winchester, and S. J. Yennello
Department of Chemistry and Cyclotron Laboratory, Texas A & M University, College Station, Texas 77843

R. G. Korteling
Department of Chemistry, Simon Fraser University, Burnaby, British Columbia, Canada V5A 1S6

L. Pienkowski
Heavy Ion Laboratory, Warsaw University, 02-093 Warsaw, Poland

H. Breuer
Department of Physics, University of Maryland, College Park, Maryland 20742

B. Back
Physics Division, Argonne National Laboratory, Argonne, Illinois 60439

S. Gushue and L. P. Remsberg
Department of Chemistry, Brookhaven National Laboratory, Upton, New York 11973

M. J. Huang, W. G. Lynch, M. B. Tsang, and H. Xi
Department of Physics and NSCL, Michigan State University, East Lansing, Michigan 48824
(Received 19 December 2000; revised manuscript received 1 June 2001; published 6 November 2001)

The relation between excitation energy and reaction observables has been examined for (6.0–14.6)-GeV/c protons, (5.0–9.2)-GeV π^-, and 8.0-GeV/c antiprotons incident on a ^{197}Au target. Relative to proton and π^- beams, 8.0-GeV/c antiprotons are found to be the most effective projectile for depositing high excitation energies in the targetlike residue. For protons and π^- the excitation-energy distributions are nearly identical and appear to be independent of beam momentum above 6–8 GeV/c. It is found that total measured charge, total thermal energy, and total charged-particle multiplicity scale most directly with excitation energy, whereas IMF multiplicity and total transverse energy exhibit large fluctuations. Correlations of the observed fragment multiplicity, charge, and kinetic-energy distributions with excitation energy indicate a transition in the reaction observables near $E^*/A \approx 4-6$ MeV. These experimental signals are consistent with a multifragmentation mechanism that becomes the dominant deexcitation mode above in the range $E^*/A \sim 4-6$ MeV.

DOI: 10.1103/PhysRevC.64.064604 PACS number(s): 25.70.Pq, 25.40.−h, 25.43.+t, 25.80.Hp

*Present address: Département de Physique, Université Laval, Laval, Quebec, Canada G1R 2J6.
[†]Present address: Laboratoire de Physique Corpusculaire de Caen, F-14050 Caen Cedex, France.
[‡]Present address: Los Alamos National Laboratory, Los Alamos, NM 87545.
[§]Present address: Rush Presbyterian, St. Luke Medical Center, Chicago, IL 60612.
[‖]Present address: Epsilon, Inc., Dallas, TX 75240.
[¶]Present address: Lawrence Berkeley Laboratory, Berkeley, CA 94720.
**Present address: Department of Physics, Cambridge University, Cambridge, U.K.
[††]Present address: Barnes Hospital, Washington University, St. Louis, MO 63130.
[‡‡]Present address: Microcal Software, Inc., One Roundhouse Plaza, Northampton, MA 01060.
[§§]Present address: Mallinckrodt Institute of Radiology, Washington University, St. Louis, MO 63110.

I. INTRODUCTION

During the past decade many challenging new physics questions have been exposed by the studies of nuclear multifragmentation; i.e., the breakup of highly excited nuclei into multiple clusters and nucleons. Motivated by the desire to define the parameters of the nuclear equation of state and to understand the physics of neutron star condensation [1], experimentalists have sought to resolve several crucial issues relevant to the properties of hot nuclear matter [2]. Can equilibrated systems be clearly identified? Is there evidence for a liquid-gas phase transition? What can the data tell us about nuclear compressibility? Is it possible to relate data from finite systems observed in the laboratory to the infinite systems that presumably occur in neutron stars? Many different physical effects—heat content, temperature, the compression/decompression cycle, rotational and shape degrees of freedom—must be understood in order to arrive at a meaningful description of the thermodynamic properties of hot nuclei.

Isolation of the thermal component of the multifragmentation process is basic to these studies and is achieved most transparently via systems prepared with GeV hadron beams [3–9]. Transport calculations indicate that the internal heating in hadron-induced reactions is created by π-N and N-N scattering and $\mathbf{\Delta}(N^*)$ resonance excitation/ pion reabsorption, which heat the targetlike residue on a time scale $\tau \lesssim 30$ fm/c, at the same time leaving it in a state of depleted density [10–14]. Further, hadron beams suppress the collective effects of the compression/decompression cycle, rotation, and the shape degree of freedom. Boltzmann-Uehling-Uhlenback calculations [14] indicate that the average entropy per nucleon becomes nearly constant after about 30 fm/c, suggesting that at least quasiequilibrium is achieved on a very fast time scale. Schematically, it is possible to perform a separation of the reaction into fast cascade and subsequent statistical deexcitation stages, providing a rationale for interpretation of these reactions in terms of hybrid two-step nonequilibrium/equilibrated decay models [15]. However, it is clear that time evolution of the targetlike residue cannot be ignored in these processes [15,16].

Hadron-induced reactions on heavy nuclei $(h+A)$ also present several experimental advantages for the study of multifragmentation and the possible relation of such events to a nuclear liquid-gas phase transition. First, only a single

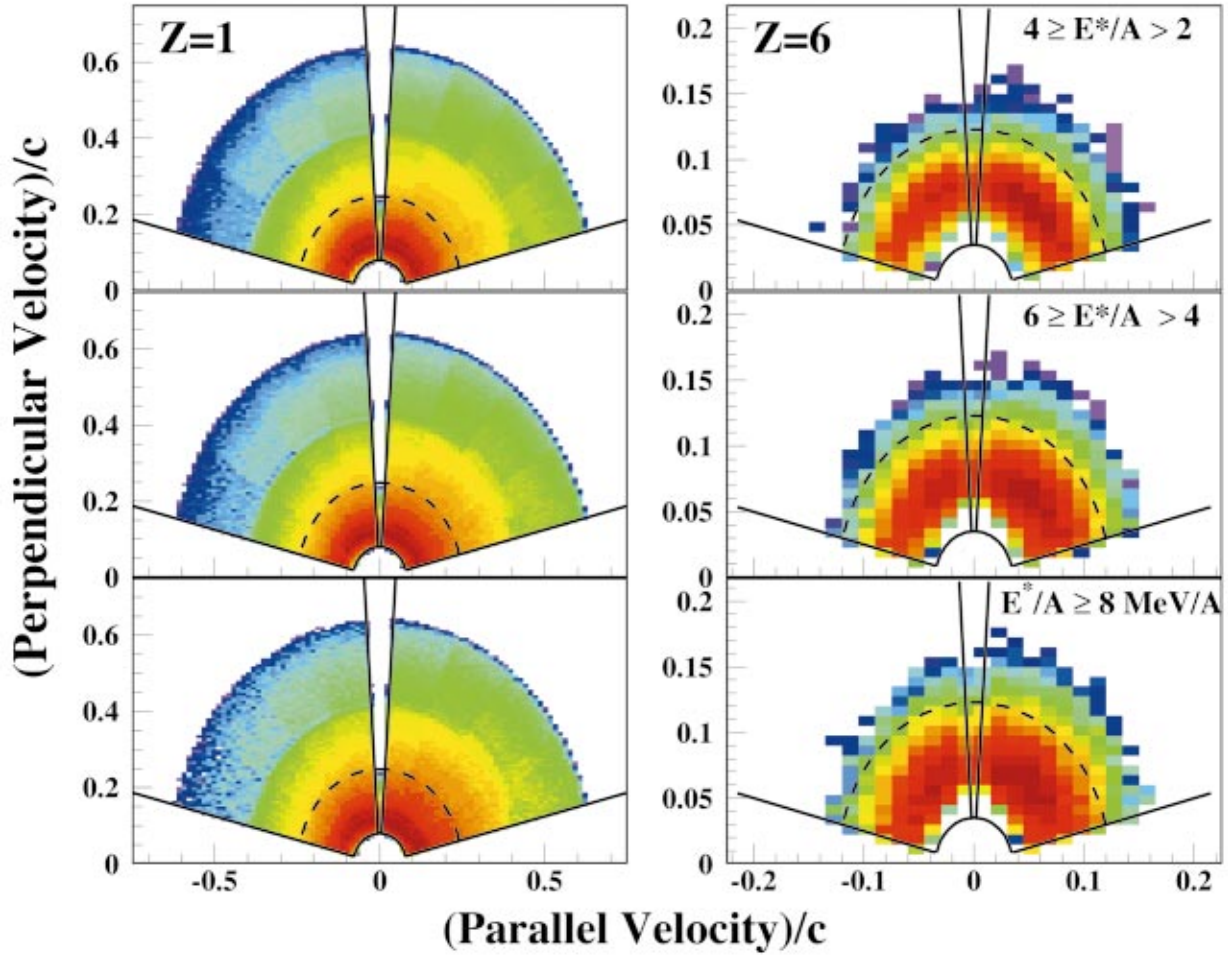

FIG. 1. (Color) Contour plot of longitudinal $v_{\parallel}$ vs transverse $v_{\perp}$ velocity of hydrogen (left) and carbon (right) fragments from the 8.0-GeV/c $\pi^- + {}^{197}$Au reaction for several bins in E^*/A. Solid lines indicate geometrical acceptance of the ISiS array; dashed line gives the thermal cutoff velocity [34], not corrected for source velocity.

TABLE I. Percent of events with at least one thermal particle of charge Z. Trigger requires at least three charged particles including one thermal particle with $Z \geqslant 2$, in silicon detectors.

Beam	Events analyzed	%($Z=1$)	%($Z=2$)	%($Z=3$)	%($Z \geqslant 3$)
5.0 GeV π^-	1.0×10^6	94.6	96.2	18.9	38.4
8.0 GeV π^- [a]	2.5×10^6	93.3	95.2	21.4	42.2
8.2 GeV π^-	2.4×10^6	94.0	96.3	19.5	38.7
9.2 GeV π^-	1.4×10^6	95.1	96.3	20.9	41.5
6.2 GeV p	2.4×10^5	94.9	96.3	18.9	38.1
10.2 GeV p	1.7×10^6	94.8	96.3	20.8	41.5
12.8 GeV p	1.4×10^6	95.2	96.4	22.0	39.2
14.6 GeV p	1.1×10^6	92.5	96.2	20.0	39.2
8.0 GeV $\bar{p}$ [a]	5.5×10^4	91.6	95.2	21.4	42.4

[a]Tagged beam.

source of thermal-like fragments is produced, as illustrated by the invariant cross-section plots in Fig. 1 for $Z=1$ and 6 fragments as a function of source excitation energy per nucleon, E^*/A. Further, the hot residues formed in $h+A$ reactions are characterized by low velocities ($v_\parallel \lesssim 0.01\ c$), permitting the breakup of the system to be studied in a frame very close to the center of mass. The comparison between $Z=1$ and $Z=6$ invariant cross sections in Fig. 1 also illustrates another important feature; i.e., the thermal-like fragments (enclosed by dashed lines) are emitted nearly isotopically, in contrast with the energetic forward-focused component observed for $Z=1$ particles, which we attribute to fast nonequilibrium processes. These features of the reaction observables play an important role in evaluating the excitation energy/nucleon, E^*/A of the hot residue.

Excitation-energy distributions for hadron- and ^{3}He-induced reactions have recently been investigated by two experimental groups. At beam energies below 2 GeV the Berlin-neutron-ball/silicon-ball [17] array has been used to study stopped- and 1.2-GeV $\bar{p}$-induced reactions at the CERN LEAR facility [7,18,19] and the ORION neutron ball has been employed at LNS Saclay to study proton- and ^{3}He-induced reactions [20,21]. These measurements have demonstrated that Au-like nuclei can survive as self-bound systems up to $E^* \sim 800-1000$ MeV, subsequently decaying via the classical low-energy mechanisms of evaporation and fission. The highest excitation energies in these experiments roughly correspond to the threshold for opening of the multifragmentation channel, as predicted [22–24] and shown experimentally [16,25,26].

At higher incident energies the Indiana silicon sphere (ISiS) array [27] has studied (1.8–4.8)-GeV ^{3}He-induced reactions at LNS Saclay [28–30] and (6.0–14.6)-GeV/c proton, 8.0-GeV/c antiproton, and (5.0–9.2)-GeV/c π^- reactions at the Brookhaven AGS [6,8,9,31]. These latter measurements have shown that at higher beam momenta about 100 mb of the cross section goes into events with $E^* > 1000$ MeV, which decay primarily via multiple light charged particle (LCP: H and He isotopes) and, IMF ($3 \leqslant Z \lesssim 20$) emission and exhibit features consistent with statistical multifragmentation models [22–24]. The ISiS results also show many characteristics in common with the ALADIN peripheral Au and Au studies [32] and the EOS ^{197}Au+ ^{12}C measurements [33], although some differences exist.

The primary objective of this paper is to investigate the relationship between the excitation energies derived in [34] and experimental observables. The data were taken at the Brookhaven National Laboratory AGS accelerator using the ISiS array, details of which are described in [34]. The number of events that met the hardware trigger of three silicon fast signals, at least one of which is a thermal $Z>1$ fragment, are summarized in Table I for each beam. For all probabilities quoted in the text, the total number of events in Table I is normalized to a unit probability, $\Sigma_i Pi(N_i)=1$.

The approach of the paper is as follows. In Sec. II the collision stage of the reaction is examined as it relates to excitation-energy deposition as a function of hadron type and beam momentum. In Sec. III, the relationship between fragment observables and excitation energy is presented. In Sec. IV, the conclusions, we discuss the correspondence of these results with the expected charactistics of a nuclear liquid-gas phase transition.

II. COLLISION DYNAMICS: PROJECTILE DEPENDENCE

Excitation-energy deposition in GeV hadron-induced reactions follows a much different path than in low-to-intermediate energy heavy-ion reactions due to the strongly forward-focused nature of the N-N collisions, formation-zone effects, and the significant transparency of nuclear matter in the GeV energy regime [35]. As a consequence of the energy dissipation mechanism, a broad range of excitation energies is populated at a single projectile incident energy. Thus, in a single reaction it is possible to study a spectrum of excited nuclei that extends from low excitation energy up to values well in excess of the total nuclear binding energy under identical experimental conditions.

Few theoretical predictions of excitation-energy deposition are available for (5–15)-GeV/c hadron-induced reac-

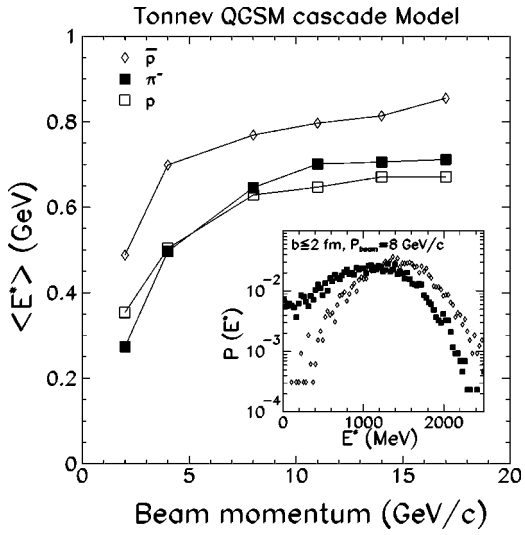

FIG. 2. INC predictions [13] of the average excitation energy for events with $E^*>50$ MeV are shown as a function of momentum for p, π^-, and $\bar{p}$ beams incident on ^{197}Au. Inset compares the excitation-energy probability distributions for 8-GeV/c π^- and $\bar{p}$ beams for central collisions ($b\leqslant 2$ fm).

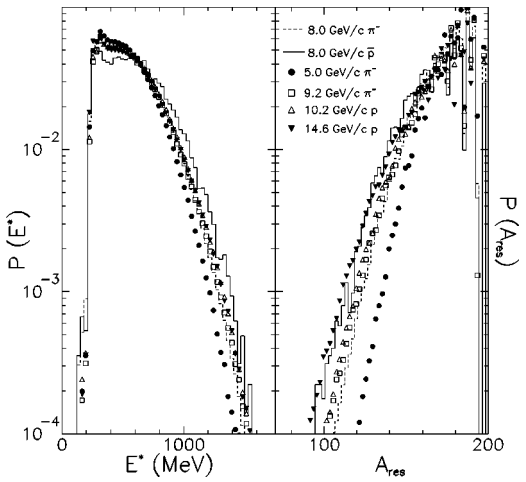

FIG. 3. Excitation-energy (left frame) and residue mass probability (right frame) distributions for several systems studied in this work, as indicated on figure. The distributions are normalized to unit probability, relative to the total number of events (Table I).

tions with heavy nuclei. Two major complications encountered in such calculations are, first, the need to incorporate all relevant scattering cross sections (many unknown) in this momentum regime, and second, the inclusion of the nuclear physics assumptions necessary to fix the amount of energy stored in the residual nucleus at the end of the fast cascade. One such model is the intranuclear-cascade (INC) code QGSM [13], which we examine here. In Fig. 2 INC calculations of the average excitation energy $\langle E^*\rangle$ imparted to Au-like residual nuclei are shown as a function of momentum for proton, π^-, and antiproton beams.

The qualitative features of the INC predictions can be summarized as follows. For protons and π^- the average excitation energy is predicted to be nearly the same. In contrast, these same calculations predict a significant increase in $\langle E^*\rangle$ for antiprotons relative to other hadrons, presumably due to the rescattering and reabsorption of some fraction of the antiproton annihilation pions ($\langle n_\pi\rangle\approx 5$). For the most central collisions ($b\leqslant 2$ fm, or $\simeq$100 mb), the calculations show a marked enhancement of high excitation-energy events for $\bar{p}$ relative to π^- beams (see inset in Fig. 2). Above a momentum of about 5 GeV/c the code also indicates a saturation in the amount of excitation energy that is deposited in the targetlike residue, a consequence of the decrease in density of the residue after shower particle emission and the hadronization time. For comparison with the INC predictions, in Fig. 3 we show the reconstructed excitation-energy and residue mass distributions for several of the systems measured in this work. Values of E^* below 250 MeV are uncertain due to the unmeasured neutrons and the requirement of three charged particles in the ISiS trigger [34]. Data for 6.2-GeV/c and 12.8-GeV/c protons (not shown) are similar to other proton and pion data in all figures.

The results in Fig. 3 confirm the qualitative behavior predicted by the INC code. Specifically, the largest population of high excitation-energy events is achieved with the 8.0-GeV/c $\bar{p}$ beam and the lowest with the 5.0-GeV/c π^- beam. In addition, the proton and π^- beams produce nearly identical E^* distributions at the same beam momentum, while the 8.0-GeV/c antiproton beam produces significantly more high excitation-energy events than does the 8.0-GeV/c π^- beam. Finally, the predicted saturation in E^* deposition is reflected by the relative insensitivity of the E^* distributions to beam momentum above about 6 GeV/c.

The residue mass A_{res} distributions in Fig. 3 show a somewhat different pattern. In this case the 14.6-GeV/c proton beam produces the lightest residues and the 5.0-GeV/c π^- the heaviest. This trend can be understood as a consequence of the initial fast cascade, which produces an increasing number of fast shower particles as the beam momentum increases ([14] and references therein). It is this process that produces the approximate saturation in average excitation energy shown in the INC calculations of Fig. 2 and the data in Fig. 3.

Quantitatively, however, the INC calculations predict E^* distributions that extend significantly beyond the data. This is shown in Fig. 4, where we compare the experimental E^* distributions for 8-GeV/c $\bar{p}$ and π^- with the INC code (stopped after $\tau=30$ fm/c). The calculation assumes random impact parameters and uses values of the code parameters that reproduce other cascade results at lower beam momenta ($\leqslant 3$ GeV/c) [37]. The two left-hand frames compare the experimentally derived excitation-energy distributions for π^- (top) and $\bar{p}$ (bottom) beams. Both the thermal definition adopted in our work [34] and the uniform spectrum cutoff of $E_i/A_{\rm IMF}<30$ MeV of [33] are shown. Although the excitation-energy enhancement with $\bar{p}$ beams relative to other hadrons is qualitatively reproduced, the INC prediction is seen to overestimate the experimentally derived excitation energies for both projectiles. In this regard, the cutoff assumption of [33] agrees better with the calculation. This agreement can be explained in terms of the inclusion of a significant number of nonequilibrium LCPs with the cutoff

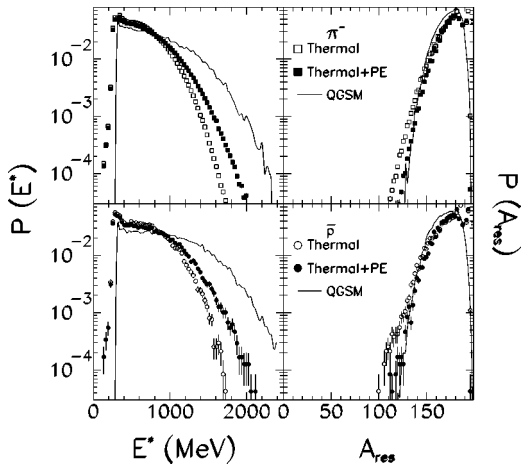

FIG. 4. Left: distribution of excitation energy in targetlike residues for π^- (upper) and $\overline{p}$ (lower) beams. Open circles denote thermal particles only, solid circles include all energies up to $E/A \leqslant 30$ MeV and lines give INC prediction [13]. Right: residue mass distributions; all symbols are the same as for left-hand panels. All distributions are normalized to unit probability.

assumption of [33], which are also included in the cascade-code excitation energies.

On the right-hand panel of Fig. 4, the mass distributions of the reconstructed residues for the 8-GeV/c π^- and $\overline{p}$ reactions are compared with the cascade code. The model predicts slightly less mass loss than deduced from the data using the thermal assumption, but is in relative accord with the results of [33], which assumes a much higher energy acceptance for thermal particles and therefore larger residues. The success in describing the residue mass while at the same time overpredicting the E^* distribution may indicate that the probability for pion rescattering and reabsorption in the residual nucleus is too high in the code and/or the formation time too short.

In order to emphasize the probability for forming highly excited systems, in Table II we examine the ratio of total events with E^* greater than a given value to that for events with $E^* \geqslant 400$ MeV. The normalization at $E^* = 400$ MeV is chosen because the sensitivity to the ISiS trigger is minimal above this energy. Table II confirms that the 8.0-GeV/c antiproton beam produces a significant enhancement of high excitation-energy events. In addition, the table shows the yield of events with excitation energy above the predicted multifragmentation threshold for Au-like nuclei (a range that spans 800–1000 MeV or about 5 MeV/nucleon) relative to total events above $E^* > 400$ MeV ($E^*/A \gtrsim 2$ MeV). The enhancement for the $\overline{p}$ beam is approximately 25% greater than the next most effective beam, 12.8-GeV/c protons. Since an increase in hadron beam momentum above 5–6 GeV/c has little effect on the amount of energy deposition, the observed enhancement of excitation energy with antiprotons suggests that the dependence of temperature on excitation energy (nuclear caloric curve) [36] could be extended to excitation energies that approach the nuclear vaporization limit by using an antiproton beam in this momentum range.

In order to convert the probabilities shown in this paper to the cross-section observed in the ISiS detector, we have attempted to estimate the missing cross section for events below $E^* < 300$ MeV as follows. We have scaled our results to both the INC predictions and the experimental results of PS208 [7]. The INC code predicts that 33% of the cross section falls below 300 MeV; when our distributions are normalized to these predictions, the value increases to 39%, since the cascade-code overestimates the highest excitation energies. For the PS208 results 49% of the cross section falls below $E^* = 300$ MeV. When normalized to our data, this number becomes 26%, since our data extend to much higher excitation energies. We adopt a value of 37% for the missing cross section and use a geometric cross section of 2100 mb, assuming $r_0 = 1.20$ fm. This gives an estimated measured cross section of $\sigma \approx 1300 \pm 200$ mb, which can be used to convert unit probability into cross section.

In summary, these studies show that, using the reconstruction procedure described in [34], excitation energies well in excess of 1 GeV can be reached in hadron-induced reactions. This translates into values up to $E^*/A \approx 9$ MeV (12 MeV) for all but the highest 1% (0.1%) of the observed events.

TABLE II. Ratio of the integrated events beyond the multifragmentation threshold for three assumed conditions ($E^* = 800$ and 1000 MeV; $E^*/A = 5$ MeV) to total events with $E^* > 400$ MeV ($E^*/A > 2$ MeV).

Beam	p(GeV/c)	T(GeV)	$\frac{P(E^*>800\text{ MeV})}{P(E^*>400\text{ MeV})}$	$\frac{P(E^*>1000\text{ MeV})}{P(E^*>400\text{ MeV})}$	$\frac{P(E^*/A>5\text{ MeV})}{P(E^*/A>2\text{ MeV})}$
$E900a\ \overline{p}$	8.0	7.2	0.30	0.097	0.27
$E900\ p$	14.6	13.7	0.23	0.067	0.21
$E900\ p$	12.8	11.9	0.25	0.076	0.22
$E900\ p$	10.2	9.3	0.23	0.066	0.19
$E900\ \pi^-$	9.2	9.1	0.21	0.058	0.17
$E900a\ \pi^-$	8.0	7.9	0.21	0.056	0.18
$E900\ \pi^-$	8.2	8.1	0.20	0.054	0.17
$E900\ p$	6.2	5.3	0.19	0.045	0.13
$E900\ \pi^-$	5.0	4.9	0.17	0.036	0.11

Increasing the proton beam momentum beyond $E_{beam} \simeq 8$ GeV does not lead to a significant increase in these values because of the nature of the energy dissipation mechanism for relativistic hadrons. Thus, the bulk of the observed cross section in these studies (90–95 %) falls below the multifragmentation threshold of $E^* \approx 800-1000$ MeV for target-like residues formed from ^{197}Au. In the next section we focus on the highest 5–10 % of the excitation-energy distribution.

III. THE EVOLUTION OF FRAGMENT OBSERVABLES WITH E^*/A

Two central questions must be addressed in order to construct an argument for a nuclear phase transition: (1) has the fragmenting system attained at least quasiequilibrium? and (2) is the evolution of the fragment observables as a function of excitation energy consistent with the expected properties of such a phenomenon? The first question can be addressed by referring to the invariant cross-section plots for hydrogen and carbon in Fig. 1. For $Z=1$ the existence of two components is evident, one consisting of fast, forward-focused particles and a second characterized by thermal-like, isotropic emission. The fast component decreases systematically with increasing fragment charge, so that for carbon (and all heavier) fragments it is negligible, as seen in Fig. 1. The slow component, bounded by the dashed lines, exhibits Maxwellian behavior and behaves similarly for all charges. When transformed into the source frame, this component is isotropic. Thus, the basic criteria for quasiequilibrium are met for the subset of events within the bounded area, which are identified as thermal particles in this text.

In the remaining section we address the second question by comparing the reconstructed E^*/A distributions from the E900 and E900a data with direct experimental observables from ISiS. Many of the examples shown here are for the 8.0-GeV/c $\pi^+ + {}^{197}$Au reaction, but other systems are nearly identical.

A. Gauges of heat content

Studies of hot nuclear matter have frequently employed various experimental observables as a measure of excitation-energy deposition (centrality) in the collision [8,20,26,30,38–43]. The choice has usually been dependent on experimental conditions, since no existing detector array is capable of simultaneously measuring all reaction products and their kinetic energies.

To examine the correlation between these observables and excitation energy, in Fig. 5 two-dimensional contour plots are shown for the 8-GeV/c $\pi^- + {}^{197}$Au reaction in which E^*/A is plotted as a function of: observed IMF multiplicity, $N_{\rm IMF}$; observed light-charged-particle multiplicity, N_{lcp}; total transverse energy, E_{tr}; total thermal energy, E_{th} as defined in [34]; total observed charge, Z_{obs}, and total bound charge, $Z_{bound}=\Sigma_i(Z_i \geqslant 2)$. Superimposed on each plot is the average value of the observable as a function of E^*/A. The plots for $N_{\rm IMF}$, N_{lcp}, E_{th}, and Z_{bound} include only thermal-like particles, inside the dashed boundary of Fig. 1

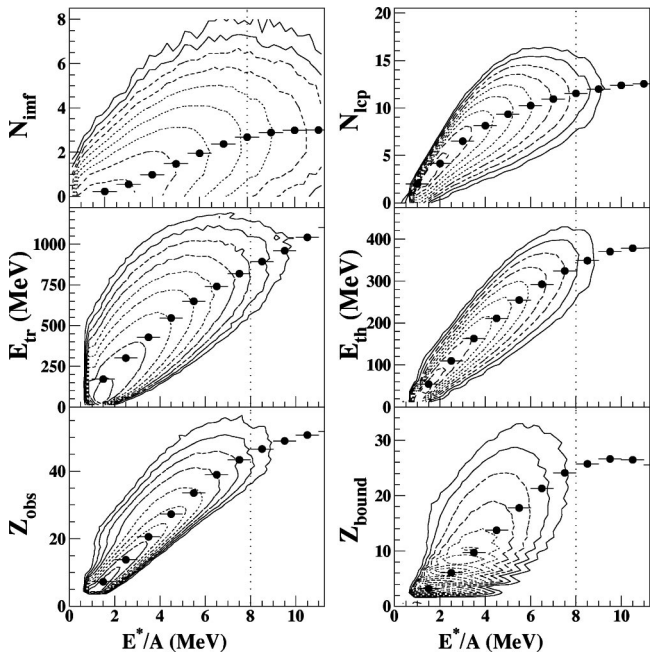

FIG. 5. Two-dimensional cross-section contours of various observables for the 8-GeV/c $\pi^- + {}^{197}$Au reaction as a function of E^*/A. Solid points are average values for each variable at a given E^*/A. Each contour line indicates a decrease of 10% in cross section and the dotted line on each graph indicates the E^*/A value above which the last 1% of the cross section is contained.

and defined in [29,34]. In evaluation of E_{tr} and Z_{obs}, all observed charged particles are included for consistency with other analyses.

For each of the average observables, a nearly linear increase with E^*/A is found up to $E^*/A \approx 8-9$ MeV. The deviation from linearity above this value is most likely due to the skewing of the distributions toward lower E^*/A, a consequence of the exponentially decreasing cross section with E^*/A, as discussed in the preceding paper [34]. However, considerable variation in the extent of the fluctuations is observed for the various parameters. As evidenced by the narrow widths of the contours, the tightest correlations occur for the total thermal energy and the total observed charge. Since the thermal energy is a significant part of the reconstructed E^* value and the total observed charge influences the reaction Q value strongly [34], a close correlation must result for these two observables. The multiplicity of light-charged particles exhibits somewhat larger fluctuations. While the Q-value contribution associated with LCP emission is large, gating on LCPs alone permits considerable variation in the reconstruction from which the total event Q value is calculated. The correlation can be improved if one looks at the total charged-particle multiplicity N_{cp} by including the IMFs in the sum, thereby constraining the Q values. Thus, these results are consistent with the use of E_{th}, Z_{obs}, and N_{cp} as excitation-energy measures of hot nuclei.

The largest fluctuations are found for the frequently used E^* markers, $N_{\rm IMF}$, and E_{tr}. The IMF multiplicity appears to be a particularly poor experimental indicator of excitation energy [44], as might be expected due to the small multi-

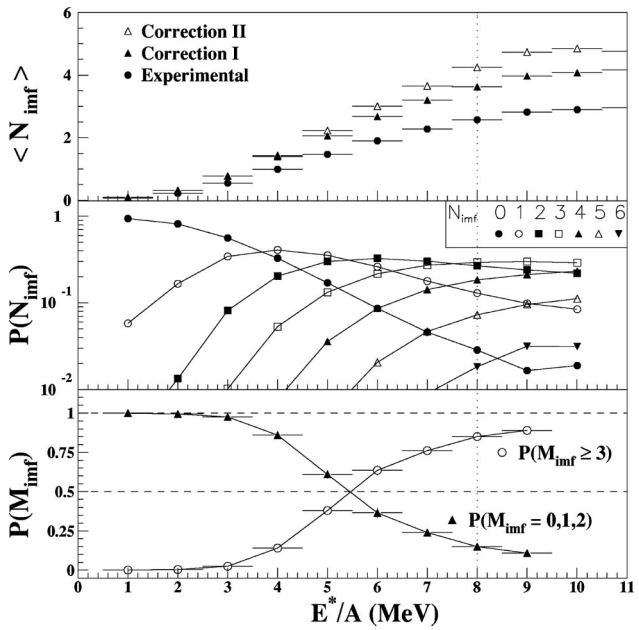

FIG. 6. Top: average number of observed IMFs (closed circles) and corrected for geometry (solid triangles) and for both geometry and fragment energy thresholds (open triangles) as a function of E^*/A for the 8-GeV/c $\pi^- + {}^{197}$Au reaction. Middle: probability for given number of detected IMFs as a function of E^*/A. Bottom: probability for IMF multiplicity $M \geqslant 3$ (circles) and $M < 3$ (triangles).

plicities. This width is also related to the small effect that IMF emission has on the Q value [34] and the large number of open channels at very high E^*/A. The large fluctuations in transverse energy are likely due to the inclusion of nonequilibrium light-charged particles in the sum. These particles originate in the cascade process during energy dissipation and are subject to the fluctuation introduced in subsequent knockout collisions. Thus, while $\langle N_{\mathrm{IMF}} \rangle$ and $\langle E_{tr} \rangle$ correlate with E^*/A, their large widths must be kept in mind when using these parameters in relation to the heat content of highly excited nuclei. Although the ISiS array does not detect heavy recoils and therefore is not ideal for determining Z_{bound}, we still find a nearly linear correlation with E^*/A; the fluctuations in this case are part of experimental origin.

B. Fragment charge distributions

The predicted opening of the multifragmentation channel in the vicinity of $E^*/A \approx 5$ MeV [22–24] indicates that multiple IMF emission should appear above this excitation energy. In Fig. 6, this prediction is examined in terms of the average IMF multiplicity, the probability for emitting a given number of IMFs, and the probability for emitting three or more IMFs relative to events with two or less. The unmeasured heavy residue is not included in these probabilities. Here N refers to the measured multiplicity and M to the true multiplicity derived from a Monte Carlo reconstruction that takes into account detector geometry and thresholds. In the top frame, the values of $\langle N_{\mathrm{IMF}} \rangle$ and $\langle M_{\mathrm{IMF}} \rangle$ increase monotonically, with no apparent deviations near $E^*/A \approx 5$ MeV. However, when the averages are decomposed into the probability for emitting a specific number of IMFs (middle frame of Fig. 6), then a different picture emerges. It is observed that as E^*/A increases, the probability for $N_{\mathrm{IMF}} = 0, 1$ decreases, while the channels for $N_{\mathrm{IMF}} \geqslant 2$ open up systematically with E^*/A.

In the bottom frame of Fig. 6, the probability for emitting three or more IMFs (the classical definition for multifragmentation [22]) is seen to grow rapidly above $E^*/A \sim 4$ MeV, while that for $M_{\mathrm{IMF}} = 0-2$ IMFs decreases correspondingly. Above $E^*/A \geqslant 6$ MeV, fragmentation into three or more IMFs becomes the dominant IMF decay channel. In this context, it should be stressed that the growth of the IMF multiplicity with E^*/A is accompanied by a corresponding growth in the light-charged-particle multiplicity, so that the fractional contribution of each to the total excitation energy remains nearly constant, as shown in the preceding paper [34]. Thus, the results of Fig. 6 demonstrate that above $E^*/A \approx 5-6$ MeV, the principal decay channel involves breakup into three or more IMFs. Below this value, the cross section is assumed to go into fission and evaporation-residue formation (the latter measured inefficiently with ISiS), as has been shown in Refs. [7,19]. These changes coincide with a rapid decrease in the relative emission time, which becomes constant at 20–50 fm/c above $E^*/A \gtrsim 5$ MeV for this system [16].

Another important aspect that must be considered in any interpretation relative to the multifragmentation mechanism is the relative charges of the emitting source and the corresponding fragments. In the top frame of Fig. 7 we show the average fraction of source charge (mass) relative to the target charge (mass) as a function of E^*/A. The values are extracted from the data by subtracting from the target charge the total charge of all shower/nonequilibrium particles, i.e., those above our thermal cutoff energy [34] and outside the dashed boundary in Fig. 1. At the highest excitation energies the effect of nonthermal particle emission is quite strong, leading to average source charges of $Z \sim 60$, i.e., a decrease of 20–30 % relative to the target.

The middle frame of Fig. 7 shows the average missing charge in our reconstruction procedure, assumed here to be a single fragment. The missing charge is obtained by subtracting the total observed charge Z_{obs} (corrected for efficiency) from the charge of the thermal-like source. This difference is then identified as $Z_{max}1$ in Fig. 7. These values should be considered upper limits, since there is a finite probability that the missing charge consists of more than a single residue, especially as the excitation energy increases. Nonetheless, comparison with the statistical multifragmentation model (SMM) [45] indicates that this is a resonable assumption [46]. The solid line in the center panel of Fig. 7 is the missing charge predicted by SMM after passing through the ISiS filter and the dashed line is the maximum fragment charge from SMM. In addition, because ISiS does not detect the small number of fast shower particles above 350 MeV, our source charge in the top frame would be slightly lower if this correction could be made. Nonetheless, the results show that above $E^*/A \approx 6$ MeV, the missing mass corresponds to an IMF, indicating that on the average the source has distintegrated completely into IMFs and LCPs.

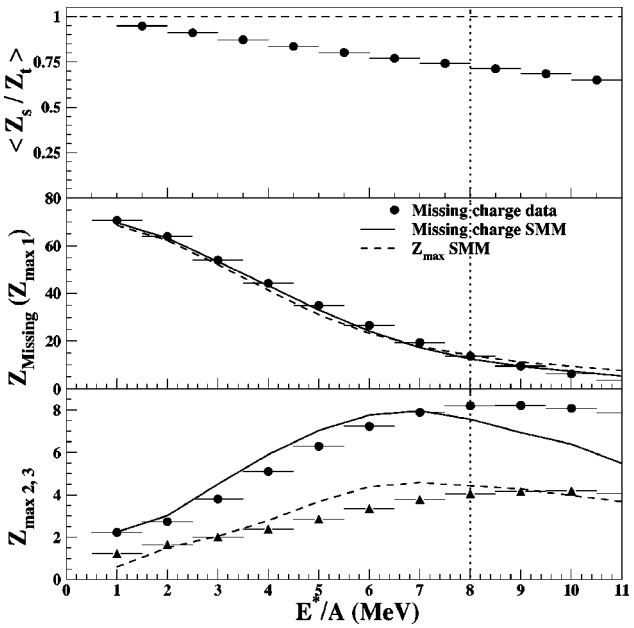

FIG. 7. Dependence of fractional source charge and IMF charges as a function of E^*/A for the 8 GeV/c-π^- + ^{197}Au reaction. Top: fractional source charge of residue. Middle: missing charge in ISiS, assumed to be the largest fragment; and SSM prediction for missing charge (solid line) and for largest fragment (dashed line), both passed through the ISiS filter. Bottom: charge of two largest observed fragments, solid line is the SMM prediction for second largest fragment ($Z_{max}2$) and dashed line for third largest fragment ($Z_{max}3$).

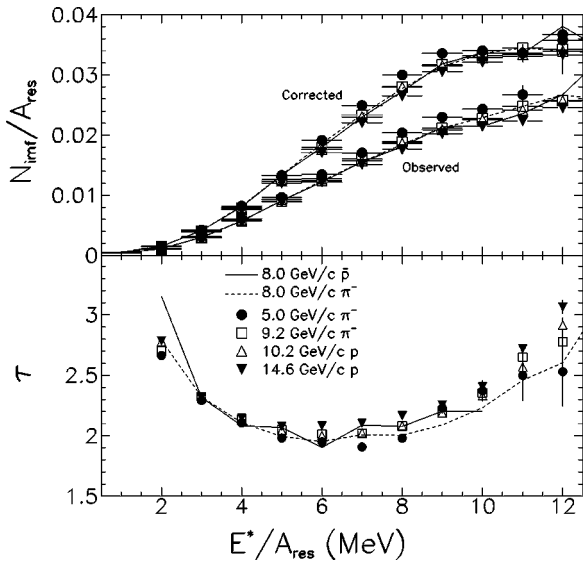

FIG. 8. Top: average ratio of observed and geometry-corrected IMFs per residue nucleon as a function of E^*/A; symbols are defined in bottom frame. Bottom: power law parameters τ from fits to the charge distributions as a function of E^*/A of the residue.

The bottom frame of Fig. 7 shows the average charge of the two heaviest observed IMFs as a function of E^*/A, or in the context of the missing charge, the second ($Z_{max}2$) and third ($Z_{max}3$) heaviest fragments in an event. It is apparent that the average charges of the fragments evolve continuously toward similar, although not completely symmetrical, values as the heat content increases. This is consistent with the behavior predicted by multifragmentation models [22–24] and with the data of [47]. The charges of the second and third largest fragments predicted by the SMM model are also shown in Fig. 7. Up to $E^*/A \lesssim 7-8$ MeV, the model and data are in relative accord. At higher excitation energies the SMM model predicts decreasing charge for the largest fragments. The version of SMM shown here stores excess excitation energy in the emitted fragments, enhancing secondary decay as E^*/A increases and increasing the relative yield of lighter fragments. The data suggest that this version of the SMM model may overestimate secondary decay effects.

Additional insight into the breakup process can be gained from studies of the fragment charge distributions, of relevance to discussions of critical phenomena and the nuclear liquid-gas phase transition [4]. The results of a power law analysis, $\sigma(Z) \alpha Z^{-\tau}$ are nearly identical for all projectiles and momenta, as shown in the bottom panel of Fig. 8. At the lowest excitation energies, values of $\tau \approx 3$ are found, consistent with lower-energy proton-induced reaction studies [48–50]. As the system is heated and particle multiplicities increase, τ values decrease steadily (larger clusters), reaching a minimum near $\tau \approx 2$ in the vicinity of $E^*/A = 6$ MeV, just above the multifragmentation threshold. This behavior is predicted by the multifragmentation models [22–24]. At still higher excitation energies, where multiplicities are large and nearly all charged particles correspond to LCPs or IMFs, τ values begin to increase. This reversal in trend toward the formation of smaller fragments at the highest excitation energies most likely reflects the influence of the excess energy above the multifragmentation threshold, due to the dissolution of large clusters in the heat bath and/or emission of highly excited clusters that subsequently undergo secondary decay.

The average number of IMFs per residue mass is found to be nearly independent of E^*/A [9], as shown in the top panel of Fig. 8. This systematic behavior is in good agreement with results from heavy-ion studies [32,51] and suggests a comparable breakup probability for hot nuclei at a given E^*/A, regardless of formation mechanism.

C. IMF kinetic-energy spectra

Finally, an important probe for estimating the breakup density in multifragment emission is provided by the IMF kinetic-energy spectra, due to the sensitivity of this observable to the Coulomb field of the emitting source. In Fig. 9 the kinetic-energy spectra for oxygen nuclei are shown at four angles for three excitation-energy bins for the 8.0-GeV/c π^- and ^{197}Au reaction. These spectra are representative of $Z \geqslant 6$ fragments observed in all systems studied here. For $Z \leqslant 6$ fragments at the lowest excitation energy, a break in the slope at high kinetic energies indicates the presence of a weak nonequilibrium component at forward angles [52]. Above $E^*/A = 4$ MeV, the kinetic-energy distributions for all $Z > 5$ IMFs can be described by a single spectral shape that is nearly independent of angle. The systematic evolution

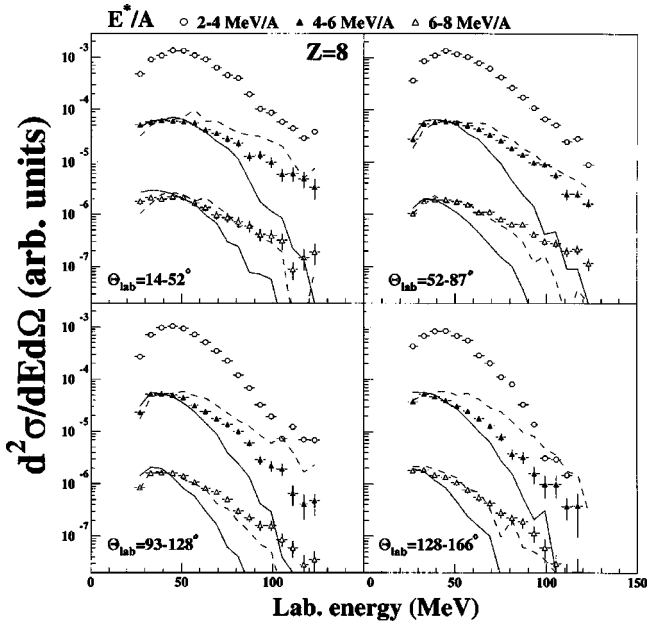

FIG. 9. Kinetic-energy spectra of oxygen nuclei at four angles in the laboratory system for three bins of excitation energy for 8 GeV/c $\pi^- + {}^{197}$Au reaction; open circles are for $E^*/A = 2-4$ MeV; closed triangles for $E/A = 4.6$ MeV; and open triangles for $E^*/A = 6-9$ MeV. The lines correspond to SMM calculations for breakup volume $V = 3V_0$ with extra expansion energy, equal to zero (solid line) and 0.5A MeV (dashed line) [53]. For each bin in excitation energy, the simulated spectrum is normalized to the maximum of the experimental one. Data are for the 8.0 GeV/c π^--induced reaction.

of the spectra with E^*/A shows that the energy of the Coulomb-like peak decreases with increasing excitation energy, as can be seen also in Fig. 1 for $Z = 6$ fragments. This behavior is consistent with the measured decrease of the

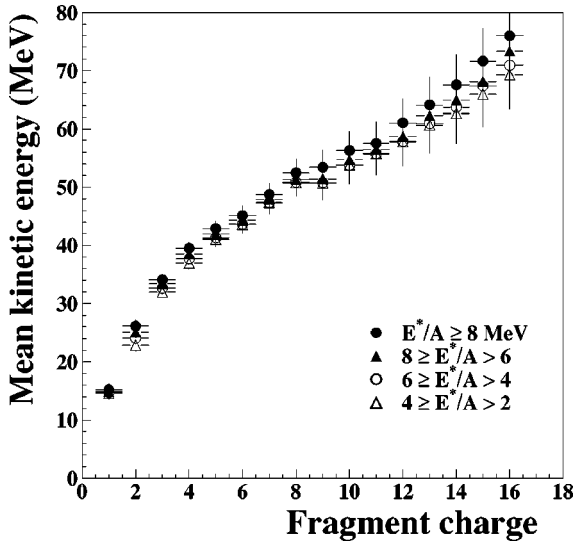

FIG. 10. Fragment mean kinetic energy as a function of IMF charge calculated in the source frame for four bins of excitation energy, as indicated on the figure. Data are from the 8.0-GeV/c π^--induced reaction.

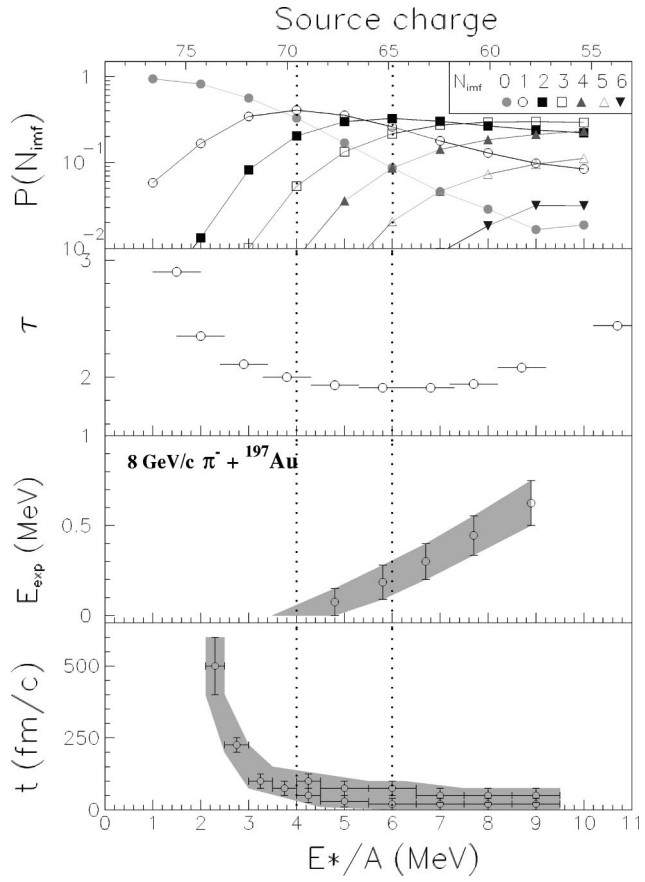

FIG. 11. Dependence on E^*/A for the following quantities, from bottom up: relative IMF emission time t, extra radial expansion energy E_{exp}/A_{IMF}, charge distribution power law exponent Z-τ, and probability for a given IMF multiplicity.

source charge (see above) and emission from an expanded/dilute system. As expected for a hotter source, the spectral slopes become flatter with increasing excitation energy.

In Fig. 10 the mean kinetic energy of fragments from the 8.0-GeV/c π^- reaction is plotted as a function of fragment charge for several excitation-energy bins, transformed into the source frame. The data are found to increase monotically with charge, as expected from Coulomb effects. But the most distinguishing feature of Fig. 10 is the near independence of the average kinetic energies on excitation energy over a broad range of E^*/A. This behavior can be interpreted within the context of Fig. 9. It results from a compensation between competing factors in which the decrease of the source charge and density (shown by the decrease of the location of the Coulomb peak) is offset by the increase in temperature of the system (flatter slope) at high excitation energy.

Also shown in Fig. 9 are SMM predictions that show the effects of extra expansion energy, as discussed in [53]. The extra expansion energy is defined here as the difference between the observed kinetic-energy spectrum and that predicted by SMM. Two reference calculations are given, one with no extra expansion energy (solid line) and another with an additional 0.5 A of energy. In Fig. 11 the extra expansion energy that must be included in the SMM in order to provide a best fit to the data is shown as a function of E^*/A. The

results indicate that the extra expansion effect increases monotonically with excitation energy, but is much smaller than in heavy-ion-induced reactions.

IV. SUMMARY AND CONCLUSIONS

In experiments E900 and E900a the collision dynamics and multiple fragment breakup features have been investigated for GeV hadron-induced reactions on ^{197}Au. Direct observables have been correlated with excitation energies determined from high statistics data obtained with the ISiS array, which measures exclusive charged-particle spectra for $1 \leqslant Z \lesssim 16$ fragments with excellent spectral definition and large dynamic range.

The reconstructed E^* distributions indicate that relative to protons and pions, 8.0-GeV/c antiprotons provide the highest-energy deposition values for the same beam momentum. For proton and π^- beams the excitation-energy distributions are nearly identical, indicating an independence of hadron type on E^* deposition. Above beam momenta of 6–8 GeV/c, the E^* distributions show little change, presumably due to increasing transparency, formation-zone effects, and depleted density of the residue. However, E^*/A values increase slightly with beam momentum due to the decreased residue charge associated with increased particle knockout at the higher momenta. The observed trends are in good qualitative agreement with the intranuclear-cascade code QGSM, although quantitatively the code overpredicts E^* deposition.

As signatures of E^* deposition, the total thermal energy, total observed charge, and total charged-particle multiplicity correlate most strongly with E^*/A, while rather large fluctuations are observed for the IMF multiplicity and total transverse energy. While the number of IMFs is not a good gauge of deposited excitation energy, multiple IMF emission is nonetheless an important signature of the multifragmentation mechanism [22–24]. Further, on average 4–5 LCPs are emitted per IMF. Thus, when total charged-particle emission is taken into account, multiple IMF events represent a process in which the nucleus has undergone a high degree of fragmentation. The excitation energy above which multiple IMF emission ($M_{IMF} \geqslant 3$) begins to dominate the yields occurs near $E^*/A \sim 5$ MeV. The decreasing amount of missing charge (assumed largest fragment) also supports the concept of a multifragmentation mechanism, e.g., the missing charge from our reconstruction procedure corresponds to an IMF at excitation energies $E^*/A \gtrsim 7$ MeV. Further consistency is evidenced by the fragment charge distributions, which evolve systematically toward larger fragments up to $E^*/A \sim 5-6$ MeV, but at higher excitation energies lighter fragments are again favored, presumably due to the secondary decay of hot primary fragments.

The IMF kinetic-energy spectra suggest an evolution from emission at normal density to a decay scenario consistent with a system at lower than normal density. This behavior is most apparent in the broadening of the spectra peaks toward low energies (lower Coulomb field) and flattening of the slopes as E^*/A increase (higher temperature). As a result, the average IMF kinetic energies show little change as a function of E^*/A.

In Fig. 11 several features of the E900/E900a results are compared to illustrate the evolution of the disintegration process with increasing excitation energy. Both the IMF multiplicity data (top frame) and charge distribution parametrization (second frame) suggest a transition in the reaction mechanism in the region $E^*/A = 4-6$ MeV. The third frame shows the deduced extra thermal expansion energy derived from the fragment spectra [53], indicating an onset near $E^*/A \simeq 5$ MeV. Finally, in the bottom frame time scale results from an IMF-IMF correlation analysis [16] show a rapidly decreasing relative emission time up to $E^*/A \approx 4$ MeV, after which a constant value of $\tau \sim 20-50$ fm/c is reached. These very short relative emission times correspond to a near-simultaneous breakup of these highly excited systems. These features of the data above $E^*/A \gtrsim 5$ MeV coincide phenomenologically with a process that is suggestive of a liquid-gas phase transition [22–24].

ACKNOWLEDGMENTS

The authors thank R. N. Yoder, R. T. de Souza, J. Vanderwerp, W. Lozowski, and K. Komisarcik, at Indiana University and P. Pile, J. Scaduto, L. Toler, J. Bunce, J. Gould, R. Hackenberg, C. Woody, W. McGahern, F. Kubasiuk, and T. Mruczkowski at AGS for their assistance with these experiments and V. Toneev, A. Botvina, and D. Durand for use of their model simulations. This work was supported by the U.S. Department of Energy and U.S. National Science Foundation, the National Sciences and Engineering Research Council of Canada, the Polish State Committee for Scientific Research, and the Robert A. Welch Foundation.

[1] H. Mueller and B.D. Serot, Phys. Rev. C **52**, 2072 (1995).
[2] See, for example, in *Proceedings of International Workshop on Gross Properties of Nuclei and Nuclear Excitations: Multifragmentation, Hirschegg, Austria, 1999*, edited by H. Feldmeier, J. Knoll, W. Nörenberg, and J. Wamback (GSI, Darmstadt, 1999).
[3] A.S. Hirsch *et al.*, Phys. Rev. C **29**, 508 (1984).
[4] N.T. Porile *et al.*, Phys. Rev. C **39**, 1914 (1989).
[5] V. Lips *et al.*, Phys. Rev. Lett. **338**, 141 (1994).
[6] W-c. Hsi *et al.*, Phys. Rev. Lett. **79**, 34 (1997).
[7] F. Goldenbaum *et al.*, Phys. Rev. Lett. **77**, 1230 (1996).
[8] T. Lefort *et al.*, Phys. Rev. Lett. **83**, 4033 (1999).
[9] L. Beaulieu *et al.*, Phys. Lett. B **463**, 159 (1999).
[10] Y. Yariv and Z. Fraenkel, Phys. Rev. C **20**, 2227 (1979); **24**, 488 (1981).
[11] D. Strottman and W.R. Gibbs, Phys. Lett. **149B**, 288 (1984).
[12] J. Cugnon, Nucl. Phys. **462**, 751 (1987); J. Cugnon, T. Mizutani, and J. Vandermuelen, Nucl. Phys. **A352**, 505 (1981); J. Cugnon, Phys. At. Nucl. **57**, 1075 (1994).
[13] V. Toneev, N.S. Amelin, K.K. Gudima, and S.Yu. Sivoklokov,

Nucl. Phys. **A519**, 463c (1990).
[14] G. Wang, K. Kwiatkowski, V.E. Viola, W. Bauer, and P. Danielewicz, Phys. Rev. C **53**, 1811 (1996).
[15] K. Kwiatkowski, W.A. Friedman, L.W. Woo, V.E. Viola, E.C. Pollacco, C. Volant, and S.J. Yennello, Phys. Rev. C **49**, 1516 (1994).
[16] L. Beaulieu *et al.*, Phys. Rev. Lett. **84**, 5971 (2000).
[17] J. Galin and U. Jahnke, J. Phys. G **20**, 1105 (1994); P. Figuera, W. Bohne, B. Drescher, F. Goldenbaum, D. Hilscher, U. Jahnke, B. Lott, L. Bienkowski, and P. Ziem, Z. Phys. A **352**, 315 (1995).
[18] D. Polster *et al.*, Phys. Rev. C **51**, 1167 (1995).
[19] U. Jahnke *et al.*, Phys. Rev. Lett. **83**, 4959 (1999).
[20] L. Pienkowski, Phys. Lett. B **336**, 147 (1994).
[21] X. Ledoux *et al.*, Phys. Rev. C **57**, 2375 (1998).
[22] J.P. Bondorf *et al.*, Nucl. Phys. **A443**, 221 (1985).
[23] W.A. Friedman, Phys. Rev. C **42**, 667 (1990).
[24] D.H.E. Gross, Rep. Prog. Phys. **53**, 605 (1990).
[25] G. Bizard *et al.*, Phys. Lett. B **302**, 162 (1993).
[26] M. Louvel *et al.*, Nucl. Phys. **A559**, 127 (1993).
[27] K. Kwiatkowski *et al.*, Nucl. Instrum. Methods Phys. Res. A **360**, 571 (1995).
[28] K.B. Morley *et al.*, Phys. Rev. C **54**, 737 (1996).
[29] E. Renshaw Foxford *et al.*, Phys. Rev. C **54**, 749 (1996).
[30] K. Kwiatkowski *et al.*, Phys. Lett. B **423**, 21 (1998).
[31] W.-c. Hsi *et al.*, Phys. Rev. C **60**, 014609 (1999).
[32] A. Schüttauf *et al.*, Nucl. Phys. **A607**, 457 (1996).
[33] J.A. Hauger *et al.*, Phys. Rev. Lett. **77**, 235 (1996); Phys. Rev. C **62**, 024616 (2000).
[34] T. Lefort *et al.*, Phys. Rev. C **64**, 064603 (2001), preceding paper.
[35] W. Busza, Annu. Rev. Nucl. Sci. **38**, 119 (1988).
[36] J. Pochodzalla *et al.*, Phys. Rev. Lett. **75**, 1040 (1995).
[37] D. S. Ginger, Honors thesis, Indiana University, 1997.
[38] R.T. de Souza *et al.*, Phys. Lett. B **238**, 6 (1991).
[39] N. Marie *et al.*, Phys. Lett. B **391**, 15 (1997).
[40] J.B. Natowitz *et al.*, Phys. Rev. C **52**, R2322 (1995).
[41] V. Lips *et al.*, Phys. Rev. Lett. **72**, 1604 (1994).
[42] J. Toke *et al.*, Phys. Rev. Lett. **75**, 2920 (1995).
[43] X. Qian *et al.*, Phys. Rev. C **59**, 269 (1999).
[44] L. Phair *et al.*, Phys. Rev. C **60**, 054617 (1999).
[45] A. Botvina, A.S. Iljinov, and I. Mishutin, Nucl. Phys. **A507**, 649 (1990).
[46] T. Lefort *et al.*, in *Proceedings of XXXVIII Winter International Meeting on Nuclear Physics*, edited by I. Iori and A. Moroni (Stompato, Milan, 2000), p. 404.
[47] Kreutz *et al.*, Nucl. Phys. **A556**, 672 (1993).
[48] R.E.L. Green, R.G. Korteling, and K.P. Jackson, Phys. Rev. C **29**, 1806 (1994).
[49] S.J. Yennello *et al.*, Phys. Rev. C **41**, 79 (1990).
[50] E. Renshaw, S.J. Yennello, K. Kwiatkowski, R. Planeta, L.W. Woo, and V.E. Viola, Phys. Rev. C **44**, 2618 (1991).
[51] L. Beaulieu *et al.*, Phys. Rev. C **54**, R973 (1996).
[52] J. Wile *et al.*, Phys. Rev. C **45**, 2300 (1992).
[53] T. Lefort *et al.*, Phys. Rev. C **62**, 031604(R) (2000).